AIAA JOURNAL
Vol. 36, No. 12, December 1998

Inviscid Rotordynamic Damping Forces due to Nonaxisymmetric Tip Clearance in Turbines

Seung Jin Song*
Inha University, Inchon 402-751, Republic of Korea

An actuator disk analysis is used to examine dynamic characteristics of destabilizing tip clearance excitation forces that arise in turbines with a whirling rotor. The slope of the cross force vs whirling frequency indicates the amount of direct damping that, together with the cross stiffness, determines rotordynamic stability. Thus, damping characteristics are extracted from the dependence of lateral forces on the whirling velocity. The analysis results reveal an inviscid aerodynamic direct damping effect. Furthermore, the damping effect is seen to be entirely due to the azimuthal pressure asymmetry or azimuthal flow redistribution. In addition, this study explores the sensitivity of such ideal damping effects to turbine design parameters such as flow coefficient and axial blade gap.

Nomenclature

C_{XX} = nondimensional direct damping, $-F_{Y'}/[(Q/2R)(e/H)(\Omega R/U)]$, [1]
C_{XY} = nondimensional cross damping, $-F_{X'}/[(Q/2R)(e/H)(\Omega R/U)]$, [1]
c = absolute flow velocity, m/s
D = turbine mean diameter, $2R$, m
d = axial blade gap, m
$\boldsymbol{E}_i$ = eigenvector for downstream perturbations
e = magnitude of rotor offset, m
F_X = lateral force in the direction of a static offset, N
F_Y = lateral force perpendicular to a static offset, N
f = tangential force per unit circumferential length, N
H = annulus height, $H_b + \delta$, m
H_b = rotor blade height, m
h_t = stagnation enthalpy, J/kg
$\hat{K}_j$ = complex amplitude of flow perturbations
K_{XX} = direct stiffness, $F_{X'}/[(Q/2R)(e/H)]$, [1]
K_{XY} = cross stiffness, $F_{Y'}/[(Q/2R)(e/H)]$, [1]
k = excitation coefficient, [1]
L = axial thickness of rotor hub, m
p = pressure, Pa
Q = turbine torque, J
q = mass flow per unit circumference of turbine, kg/s
R = turbine mean radius, m
R_D = turbine design reaction, [1]
t = time, s
U = turbine rotational speed at mean radius, ωR, m/s
w = relative velocity, m/s
X, Y = fixed coordinate system
X', Y' = whirling coordinate system
x = axial direction in the actuator disk model
y = azimuthal direction in the actuator disk model
y' = distance from the maximum tip gap in the azimuthal direction
z = radial direction in the actuator disk model
α = absolute flow angle, deg
β = Alford coefficient, [1]
Δ = leakage jet thickness, m
δ = radial tip clearance, m
η = turbine efficiency, [1]
θ = azimuthal angle measured in the direction of rotation from the minimum gap location, deg
λ = mass fraction of the leakage jet, [1]
ρ = density, kg/m^3
ϕ = upstream velocity potential
ϕ_D = turbine design flow coefficient, c_x/U, [1]
ψ = turbine work coefficient, $[(h_{t3} - h_{t1})/\rho U^2]$, [1]
Ω = angular frequency of rotor shaft whirl, s^{-1}
ω = angular frequency of rotor shaft rotation, s^{-1}

Subscripts

p = due to azimuthal pressure nonuniformity
T = due to combined effects of pressure and torque nonuniformity
u = value at zero tip clearance
wd = due to azimuthal work or torque nonuniformity
X, Y = fixed coordinate system
X', Y' = whirling coordinate system
0 = far upstream on the blade scale, equivalent to radius scale 0−
0− = near upstream of the actuator disk on the radius scale
0+ = near downstream of the actuator disk on the radius scale
1 = stator inlet on the blade scale
2 = in the direction perpendicular to the offset
$2r$ = rotor inlet on the blade scale
$2s$ = stator exit on the blade scale
3 = rotor exit
4 = far downstream on the blade scale, equivalent to 0+ on the radius scale

Superscripts

$\bar{}$ = azimuthal mean or axisymmetric value
$'$ = nonaxisymmetric perturbation
$\hat{}$ = complex amplitude
$+$ = downstream flow part associated with the rotor tip gap
$-$ = downstream flow part associated with the rotor blade

Introduction

OVER the years, various types of excitation mechanisms that induce rotordynamic instability, e.g., labyrinth seals and turbines, have been identified and analyzed.[1] One mechanism found in turbines is the so-called Alford force. Thomas[2] first identified this instability in steam turbines, and Alford[3] independently found the same instability in aircraft engines. However, investigations of tip-clearance-induced rotordynamic forces have been scarce, especially when compared with those of the other excitation mechanisms such as labyrinth seals (e.g., see Refs. 4 and 5).

The Alford force results from fluid–structure interaction in a turbine with nonaxisymmetric tip clearance. In a turbine with an offset rotor, higher efficiency is assumed in the smaller clearance region, resulting in a higher local torque (Fig. 1). Thus, tangential force per

Received Feb. 19, 1997; revision received June 1, 1998; accepted for publication July 15, 1998.

*Assistant Professor, Department of Aerospace Engineering, 253 Yonghyun-Dong, Nam Ku.

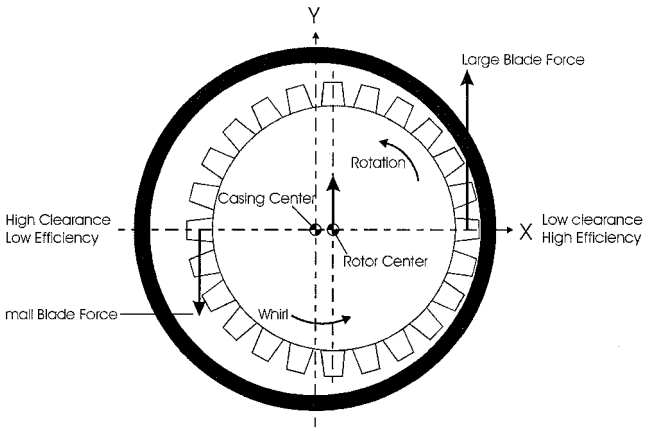

Fig. 1 Thomas–Alford destabilizing mechanism.

unit length is assumed to decrease linearly with the ratio of the local tip gap to the blade height:

$$f = f_u - \beta(\delta/H_b) \tag{1}$$

where f_u is the hypothetical value of f at zero clearance and turbine torque can be expressed as $Q = 2\pi Rf$. If a turbine rotor is statically offset by e in the X direction, varying δ/H_b leads to a force perpendicular to the direction of the offset

$$F_Y = (\beta/2)(Q/R)(e/H_b) \tag{2}$$

This force then either causes or enhances unstable forward whirling motion. By comparison, for the same static offset in the X direction, Thomas[2] assumed F_Y to be of the following form:

$$F_Y = (k_2/\eta_u)(Q/R)(e/H_b) \tag{3}$$

where η_u is the expected turbine efficiency at zero tip clearance. Referred to as the excitation coefficient in the German literature, k_2, according to Childs,[6] is related to the Alford factor as follows:

$$k_2 = \beta(\eta_u/2) \tag{4}$$

For a static offset, β is similar, though not identical, to K_{XY}. K_{XY} has the eccentricity normalized by the annulus height instead of the blade span. However, in practice, the values of H and H_b would hardly be distinguishable because tip clearance is on the order of 1% of blade span. Therefore, henceforth β and K_{XY} will be used interchangeably.

Alford[3] and other turbomachinery designers have assumed values of β to be between 1 and 1.5 primarily because the available turbine efficiency data show that slopes of the efficiency-vs-tip-clearance graph range between 1 and 1.5. Furthermore, a β value of 1 yielded realistic predictions for Childs[6] in his rotordynamic analysis of the Space Shuttle main engine (SSME).

However, investigations of turbine forces report β values much larger than 1. Urlichs[7] measured stiffness forces in an unshrouded turbine. Stiffness forces refer to forces proportional to the static rotor offset, and damping forces refer to those proportional to the rotor whirling velocity. His data show β values between 4 and 5. Martinez-Sanchez et al.[8] acquired direct and cross stiffness force data and aerodynamic data in an unshrouded turbine with an offset rotor. Cross forces act in a direction normal to the rotor offset direction, and direct forces act in the direction of the offset. Their data show β ranging from 2 to 4. Thus, the discrepancy between the β values of 1 used by practicing engineers and the values of 2–5 found in investigations strongly suggests the existence of damping forces.

Therefore, this paper analyzes rotordynamic damping effects due to aerodynamic forces in a single-stage unshrouded turbine with a whirling rotor. The analytical fluid dynamic model described by Song and Martinez-Sanchez[9,10] is used for this study. The focus is on the physical mechanisms responsible for aerodynamic damping forces. Furthermore, the influence of turbine design parameters, such as the design flow coefficient and the axial gap between the stator and rotor blades, is also investigated. The design flow coefficient was chosen because it is arguably the most important turbine design parameter. The axial blade gap was selected because lengthening it has been shown to increase β (Refs. 7 and 10).

Analytical Model

The actuator disk model collapses an unshrouded turbine stage into an actuator disk at $x = 0$ (Fig. 2). The model uses harmonic analysis to find the concentric (zeroth-order) and eccentric (first-order perturbation) solution. The model is analytical and, thus, does not require empirical input.

The analysis is limited to incompressible, inviscid flow in turbines with a high hub-to-tip ratio. Furthermore, except for the rotor tip gap, the blade geometry is assumed to be radially uniform ($\partial/\partial z = 0$) and to be equivalent to that at the mean radius. Also, zero deviation is assumed, and flow conditions are radially uniform at the stator exit.

Figure 3 shows a turbine rotor simultaneously undergoing rotation and a circular whirl. Forward whirling direction is considered positive. The flow appears unsteady in the inertial frame and steady in the whirling frame. The azimuthal location of the maximum tip gap is $\Omega t + \pi$ rad from the inertial X axis. In the inertial frame, the rotor's whirling motion introduces unsteadiness:

$$\left(\frac{\partial}{\partial t}\right) = -\Omega R\frac{\partial}{\partial y} \tag{5}$$

For small tip gaps with an offset rotor, the azimuthal distribution of the rotor tip gap is given as a small perturbation about the mean value:

$$\delta = \bar{\delta} + \mathrm{Re}\{\hat{e}\ \exp[i(y/R - \Omega t)]\} \tag{6}$$

where y is the distance from the X axis. The solution procedure is summarized in the Appendix.

Figures 4 and 5, from Song and Martinez-Sanchez,[10] show, respectively, the azimuthal pressure and torque distributions predicted by the model compared with experimental data. The agreement is

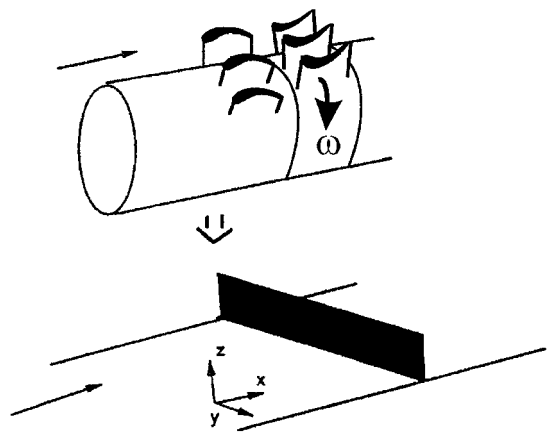

Fig. 2 Radius scale view of the actuator disk.

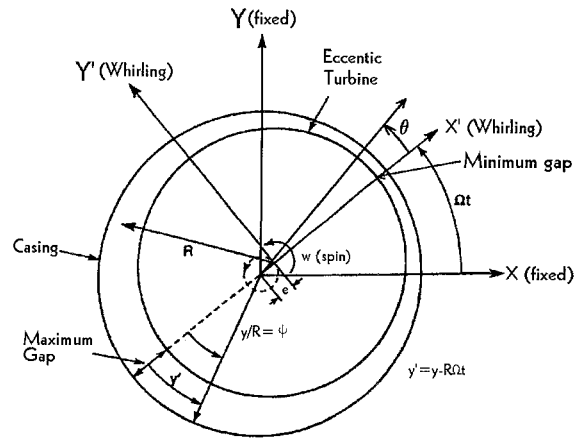

Fig. 3 Coordinate system used in the analysis.

Table 1 Predicted direct and cross stiffness for baseline turbine compared with data from Ref. 10

K_{ij}	Model/data	p	wd	Total
K_{XX}	Model	−2.0	−0.9	−2.7
K_{XX}	Data	−2.6	−0.6	−3.2
K_{XY}	Model	+1.5	+1.8	+3.2
K_{XY}	Data	+1.6	+1.9	+3.5

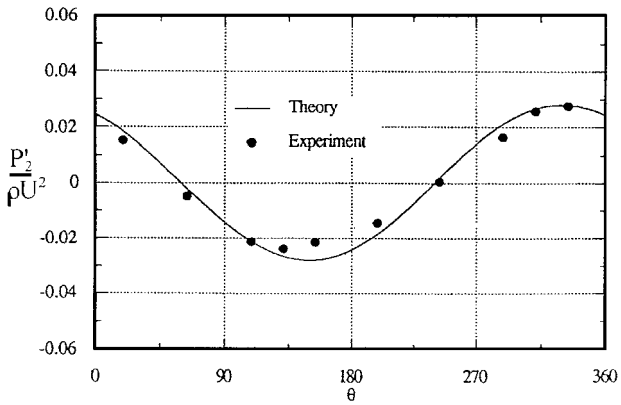

Fig. 4 Predicted and measured pressure asymmetry for baseline turbine at $e/H_b = 0.011$ (from Ref. 10).

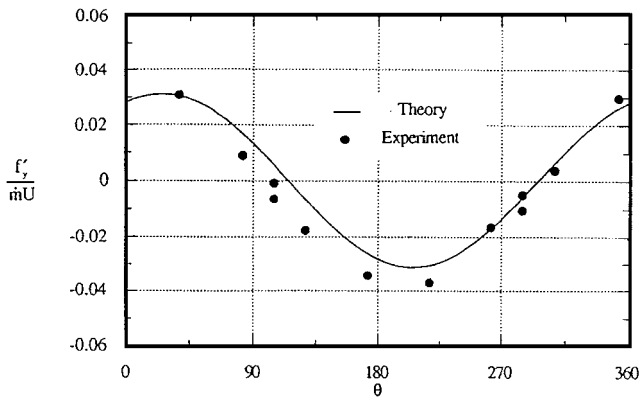

Fig. 5 Predicted and measured torque asymmetry for baseline turbine at $e/H_b = 0.011$ (from Ref. 10).

good. Both distributions show defects near the azimuthal location of 180 deg, the maximum gap location. The pressure asymmetry results from the azimuthal flow redistribution caused by nonaxisymmetric tip clearance and was not previously anticipated. The torque asymmetry accounts for about $\frac{3}{5}$ of the cross force, whereas the pressure asymmetry accounts for $\frac{2}{5}$ of the cross force and most of the direct force. The predicted and measured values of K_{ij} agree to within 25% of each other (Table 1).

Model Predictions and Discussion

This section presents the predicted nondimensional damping and stiffness for selected turbines. The first stage of the high-pressure fuel turbopump in the SSME, selected for the preceding analyses,[9,10] was chosen as the baseline turbine for this study as well. Its design flow coefficient, reaction, and nondimensional axial blade gap are 0.58, 0.21, and 0.05, respectively (Table 2). The design flow coefficient is defined as the ratio of axial velocity to turbine rotational speed at the design condition and is representative of aerodynamic loading of turbine rotor blades; a lower value means higher loading (Fig. 6). The design reaction is the ratio of the pressure drop in the rotor to that in the stage. A stage consists of stator blade row and rotor blade row. Zero reaction or impulse turbine means that all of the pressure drop occurs in the stator, whereas reaction turbine means that all of the pressure drop occurs in the rotor. Axial gap refers to the distance between the trailing edge of the stator blades and the leading edge of the rotor blades (Fig. 7).

Table 2 Baseline turbine design parameters (from Ref. 10)

Parameter	Value
R_D	0.21
ϕ_D	0.58
ψ_D	1.51
α_{2s}	70 deg
α_3	−3 deg
d/R	0.05

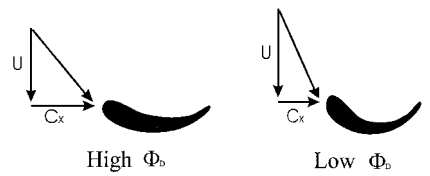

Fig. 6 High-ϕ_D and low-ϕ_D turbine rotor blade shapes.

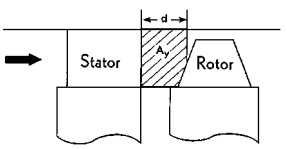

Fig. 7 Schematic showing the axial blade gap.

Nondimensional damping and stiffness are extracted as follows: A plot of nondimensional cross force vs nondimensional whirling frequency can be curve fitted with a polynomial as follows:

$$\frac{F_{Y'}}{(Q/2R)(e/H)} = a + b\left(\frac{\Omega}{\omega}\right) + c\left(\frac{\Omega}{\omega}\right)^2 \tag{7}$$

Then $K_{XY} = a$ and $C_{XX} = -b$. Similarly, nondimensional direct force can be curve fitted as

$$\frac{F_{X'}}{(Q/2R)(e/H)} = d + e\left(\frac{\Omega}{\omega}\right) + f\left(\frac{\Omega}{\omega}\right)^2 \tag{8}$$

Then $K_{XX} = d$ and $C_{XY} = -e$. According to Alford,[3] K_{XX} would be zero. A linearized stability analysis has shown that the stability of a rotor system is determined by the direct damping coefficient C_{XX} and the cross stiffness coefficient K_{XY} (Ref. 8). It is reiterated that the rotordynamic coefficients thus determined are strictly due to inviscid fluid dynamic effects because of the perfect fluid assumption in the model. Also, all of the results presented are for $e/H = 0.01$.

Effect of Design Flow Coefficient

Figure 8 shows the total nondimensional direct and cross forces vs the rotor whirling frequency for various ϕ_D. The direct force exhibits an inertia-like parabolic dependence on the whirling frequency with little cross damping, and the cross force shows a more linear dependence on the whirling frequency. Table 3 shows the values of damping and stiffness determined from curve fitting the predicted forces in Fig. 8. The magnitudes of both C_{XX} and K_{XY} decrease nonlinearly as ϕ_D increases. Positive C_{XX} and K_{XY} values indicate the stabilizing aerodynamic damping force and the destabilizing aerodynamic stiffness force, respectively. Decreasing ϕ_D leads to the penalty of higher K_{XY} but also yields the benefit of higher C_{XX}, and this trend can be seen in plots of C_{ij} and K_{ij} vs ϕ_D in Figs. 9a and 9b. Thus, not only aerodynamic performance but also susceptibility to rotordynamic instability can now be considered when selecting ϕ_D during the design stage.

As described in the model description section, the lateral forces contain components due to pressure and torque asymmetries, and Figs. 10 and 11 show the breakdown of the lateral forces in Fig. 8 into those components. Two trends should be noted. First, torque asymmetry's contribution to the lateral forces is smaller than that of the pressure asymmetry. Second, the damping effect is almost entirely due to the pressure asymmetry (Tables 4 and 5). C_{XX} and C_{XY} values due to pressure asymmetry are much larger than those due to

Table 3 Total stiffness and damping coefficients for various ϕ_D

ϕ_D	C_{XX}	C_{XY}	K_{XX}	K_{XY}
0.42	+4.22	−0.49	−4.37	+5.65
0.58	+2.08	+0.18	−2.65	+3.19
0.99	+0.67	+1.07	−1.60	+1.58

Table 4 Rotordynamic coefficients due to pressure asymmetry for various ϕ_D

ϕ_D	C_{XX}	C_{XY}	K_{XX}	K_{XY}
0.42	+4.18	+0.80	−3.01	+3.27
0.58	+1.77	+0.77	−1.83	+1.43
0.99	+0.15	+0.73	−1.05	+0.62

Table 5 Rotordynamic coefficients due to torque asymmetry for various ϕ_D

ϕ_D	C_{XX}	C_{XY}	K_{XX}	K_{XY}
0.42	+0.04	−1.29	−1.37	+2.37
0.58	+0.31	−0.59	−0.82	+1.76
0.99	+0.52	+0.34	−0.55	+0.96

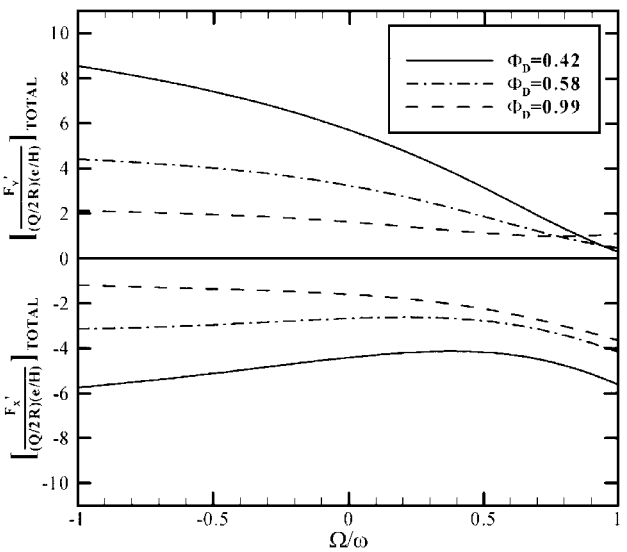

Fig. 8 Total direct and cross stiffness vs whirling frequency for ϕ_D = 0.42, 0.58, and 0.99.

torque asymmetry. Thus, under dynamic conditions, the azimuthal flow redistribution, i.e., pressure asymmetry, instead of the torque asymmetry, provides aerodynamic damping.

For axial leaving conditions, increasing ϕ_D for a fixed value of reaction means reduced loading in both the stator and the rotor. Because the loading is known to drive to the tip leakage jet, decreased loading means decreased tip-clearance-related losses. Thus, the lateral forces due to torque asymmetry effects are decreased as ϕ_D increases. Furthermore, reduction in the stator turning reduces the swirl entering the rotor; incoming swirl is proportional to $(\tan\alpha_2 - \Omega R)$. Decreased swirl leads to a decreased azimuthal pressure gradient. Also, increasing whirl frequency reduces the relative swirl entering the rotor. Thus, the magnitude of the pressure asymmetry is reduced, and Fig. 10 shows decreasing cross forces as the whirling frequency increases.

To further investigate the damping effects due to the pressure asymmetry, the influence of whirling frequency on the azimuthal flow redistribution is examined. Song and Martinez-Sanchez[10] suggest that the damping effects are due to the kinematics of whirling motion. Figure 12 shows the upstream axial velocity perturbation

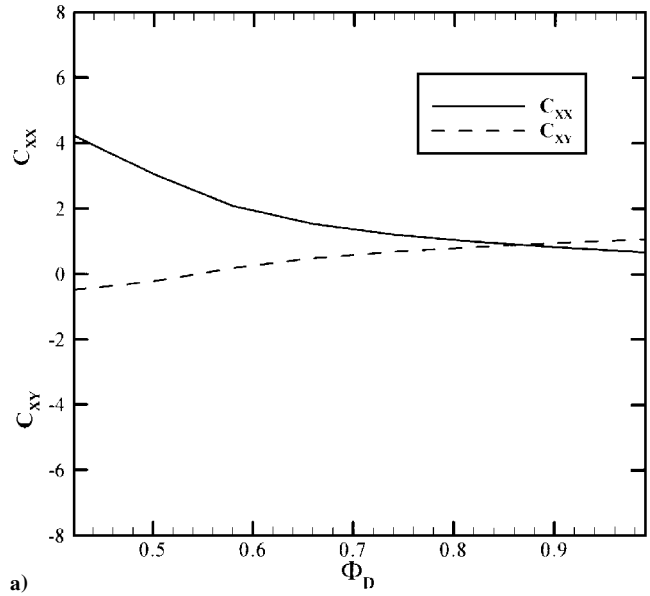

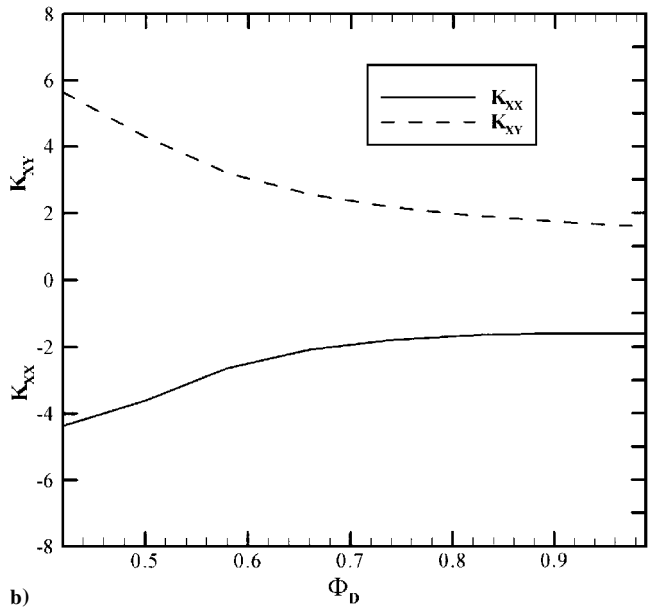

Fig. 9 Damping and stiffness vs design flow coefficient.

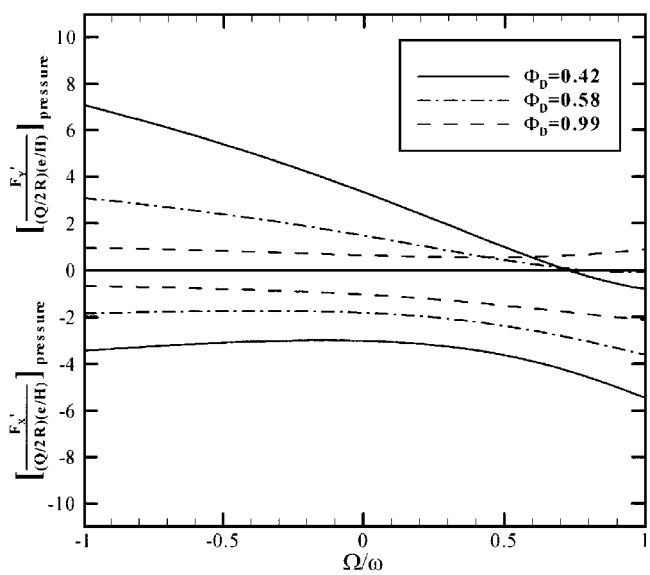

Fig. 10 Direct and cross stiffness due to pressure asymmetry vs whirling frequency for ϕ_D = 0.42, 0.58, and 0.99.

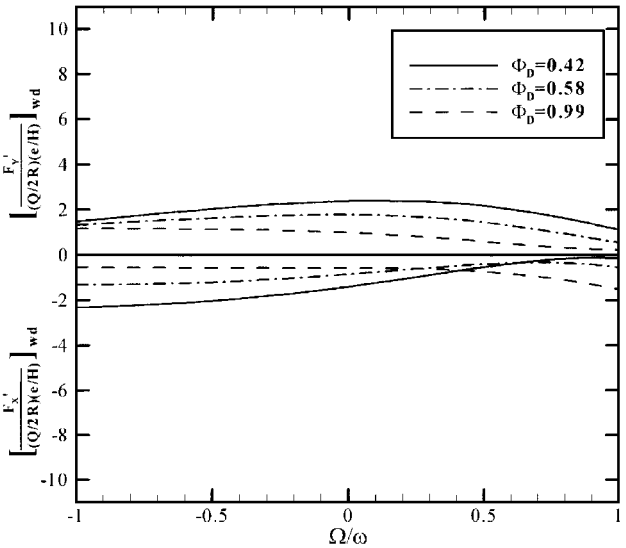

Fig. 11 Direct and cross stiffness due to torque asymmetry vs whirling frequency for $\phi_D = 0.42$, 0.58, and 0.99.

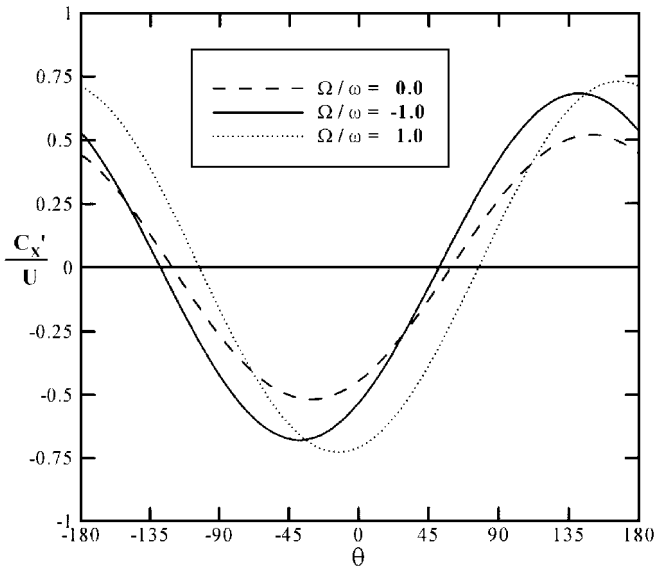

Fig. 12 Axial velocity asymmetry vs θ for $\phi_D = 0.58$.

distribution (180 deg out of phase with pressure perturbation distribution) vs θ at whirling frequencies of -1.0, 0.0, and $+1.0$ for $\phi_D = 0.58$. The azimuthal locations of maximum axial velocity, or minimum pressure, are $\theta = 140$, 149, and 167 deg, respectively. The damping effect is primarily due to changes in the azimuthal flow redistribution upstream of the stator. Thus, the kinematics of the whirling motion provides an important damping mechanism. However, the nonlinear variation of the phase angle vs the whirling speed suggests that there are other, though minor, dynamic effects at work such as perturbations in rotor exit flow angle, rotor exit mass flux, and turbine torque.

Effect of Axial Blade Gap

Next, the influence of d on the damping characteristics is examined. For a statically offset rotor, Song and Martinez-Sanchez[10] show that the axial blade gap causes azimuthal flow redistribution within the gap with two consequences. First, the lateral forces due to torque asymmetry are increased. Second, lateral forces due to pressure asymmetry are rotated, increasing the cross force and decreasing the direct force.

Figure 13 shows the total lateral forces' dependence on the whirling frequency for different axial blade gaps. As in the earlier cases, the cross forces decrease almost linearly with increasing whirling speed, indicating stabilizing damping effect. The direct forces display an inertia-like parabolic dependence on the whirling frequency. As in the statically offset rotor case, the cross forces increase and the direct forces decrease as d/R increases. However, the slopes of the forces vs the whirling frequency hardly change. This trend can be inferred from Table 6, which lists damping and stiffness values for various d/R. Thus, increasing d/R leads to the penalty of higher K_{XY} but does not gain much benefit in C_{XX}. Figures 14a and 14b, in which C_{ij} and K_{ij} are plotted vs d/R, show the trend graphically. Thus, for rotordynamic purposes, it would be prudent to maintain d as small as tolerable.

Figures 15 and 16 show the breakdown of lateral forces for various axial blade gaps into those due to the pressure and torque asymmetry, respectively. Again, the inviscid damping effect is mostly due to the pressure asymmetry. Furthermore, as in the flow coefficient case, the pressure asymmetry is caused by the upstream azimuthal flow redistribution. The torque asymmetry shows little dependence on the whirling speed. The relative contributions of pressure and torque asymmetry to damping and stiffness coefficients are given numerically in Tables 7 and 8.

The dynamic forces in turbines thus found can be compared with those in labyrinth seals as follows: First, the approximately linear decrease in the cross force due to pressure asymmetry vs whirling speed is similar to that found in labyrinth seals by Millsaps.[4] However, the decrease in the labyrinth seal force was attributed to reduction in the swirl coming into the seal gland as the whirling speed

Table 6 Total stiffness and damping coefficients for various d/R

d/R	C_{XX}	C_{XY}	K_{XX}	K_{XY}
0.01	+1.98	+0.08	−2.64	+2.65
0.05	+2.08	+0.18	−2.65	+3.19
0.10	+2.21	+0.28	−2.50	+3.83
0.20	+2.49	+0.43	−1.89	+4.81

Table 7 Rotordynamic coefficients due to pressure asymmetry for various d/R

d/R	C_{XX}	C_{XY}	K_{XX}	K_{XY}
0.01	+1.61	+0.70	−1.98	+0.95
0.05	+1.77	+0.77	−1.83	+1.43
0.10	+1.98	+0.85	−1.51	+1.96
0.20	+2.39	+1.07	−0.67	+2.65

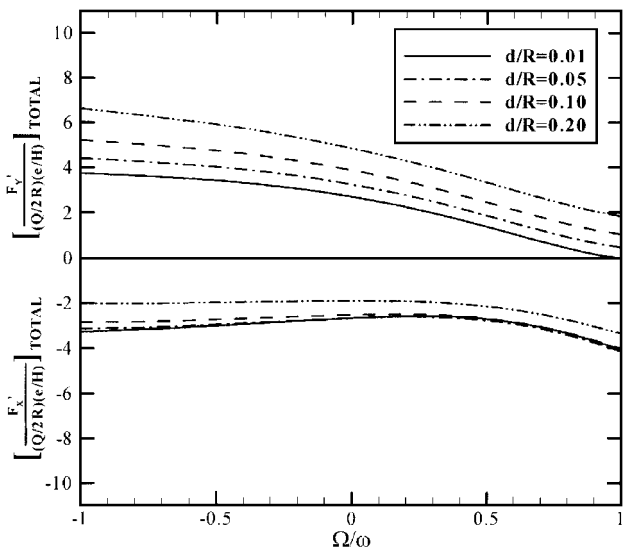

Fig. 13 Total direct and cross stiffness vs whirling frequency for $d/R = 0.01$, 0.05, 0.10, and 0.20.

Table 8 Rotordynamic coefficients due to torque asymmetry for various *d/R*

d/R	C_{XX}	C_{XY}	K_{XX}	K_{XY}
0.01	+0.37	−0.62	−0.66	+1.70
0.05	+0.31	−0.59	−0.82	+1.76
0.10	+0.23	−0.57	−0.99	+1.87
0.20	+0.10	−0.64	−1.22	+2.16

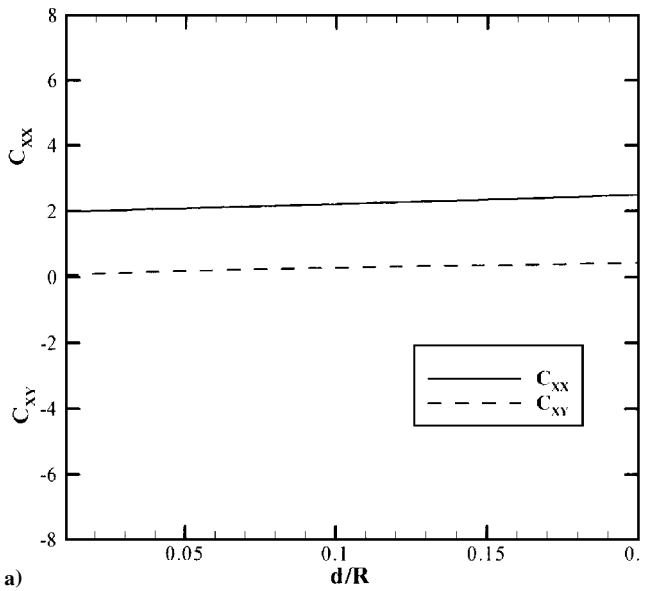

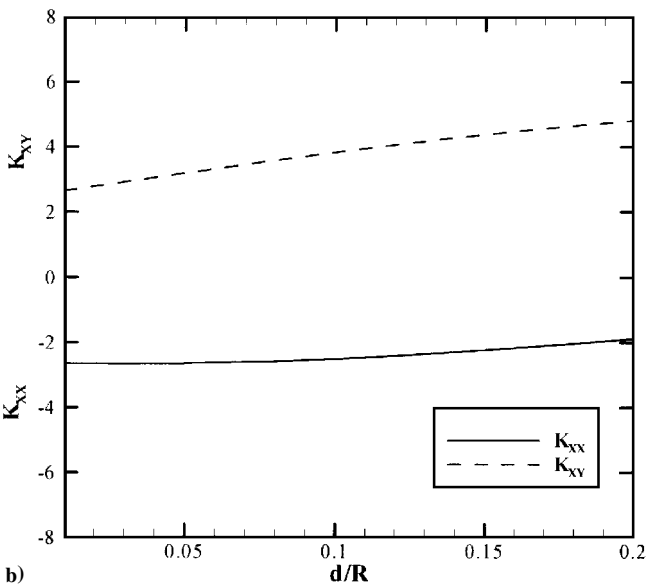

Fig. 14 Damping and stiffness vs axial blade gap.

increased. Therefore, this mechanism is different from the upstream azimuthal flow redistribution mechanism found in turbines. Second, decreasing flow coefficient in turbines leads to results similar to those caused by increasing the pressure ratio across the seal; both direct damping and cross stiffness are increased. Third, increasing the axial blade gap in turbines and reducing the rotation rate in seals both increase cross stiffness without affecting direct damping. Thus, different mechanisms lead to similar gross trends in rotordynamic coefficients of turbines and seals.

Finally, the results would explain why the K_{XY}, or the β, value of about 1 yielded realistic predictions for Childs[6] in his rotordynamic analysis of the SSME. According to Ek,[11] the instability that delayed the Shuttle's SSME development occurred at about 0.5–0.6 of the shaft speed. Figure 8 shows that the nondimensional cross force has

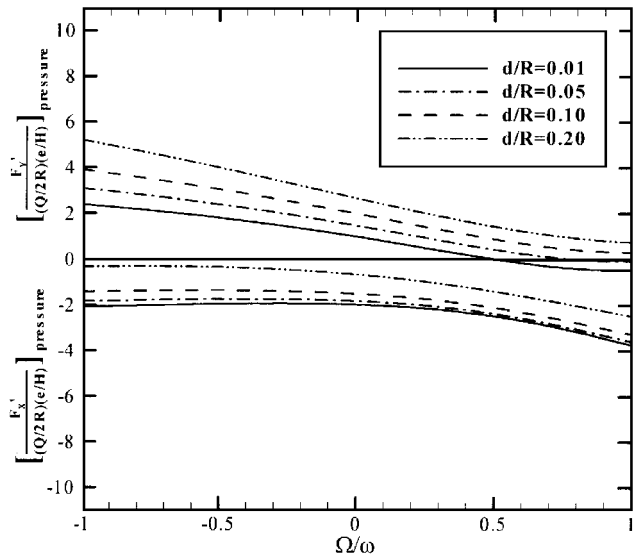

Fig. 15 Direct and cross stiffness due to pressure asymmetry vs whirling frequency for *d/R* = 0.01, 0.05, 0.10, and 0.20.

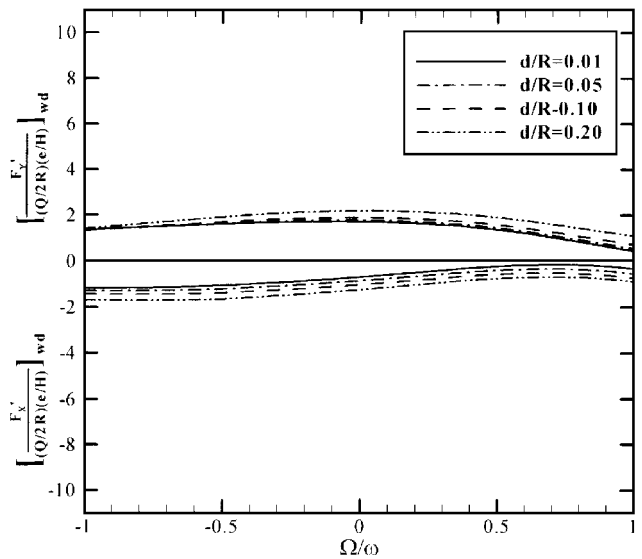

Fig. 16 Direct and cross stiffness due to torque asymmetry vs whirling frequency for *d/R* = 0.01, 0.05, 0.10, and 0.20.

a value of approximately 1.5 between the whirling frequencies 0.5 and 0.6.

Conclusions

The aerodynamic stiffness and damping forces caused by asymmetric tip clearance in an axial turbine with a whirling rotor have been analyzed. The focus is on the dynamic characteristics of the cross force. Furthermore, the dependence of such forces on the turbine design flow coefficient and the axial blade gap has been examined. Based on the analytical results, the following new conclusions can be drawn:

1) An inviscid, stabilizing aerodynamic direct damping mechanism exists in a turbine with a whirling rotor. As the whirling speed increases, the cross force decreases in magnitude.

2) Almost all of the direct damping effect is due to changes in the azimuthal flow redistribution, i.e., pressure asymmetry, relative to the whirling rotor. Torque variation, the mechanism originally envisioned by researchers, plays a negligible role in damping.

3) The azimuthal flow redistribution results mainly from the kinematics of the whirling rotor as the flow redistributes in response to the continuously varying tip clearance.

4) Increasing the design turbine loading, or decreasing the design turbine coefficient, leads to not only larger cross stiffness force but also larger direct damping force.

5) Lengthening the axial blade gap between the stator and the rotor also increases the cross stiffness force but does not significantly affect the direct damping force.

6) For improved rotordynamic performance, highly loaded turbine blading with stator and rotor blade rows placed far apart should be avoided.

Appendix: Actuator Disk Model

This appendix contains a brief description of the model of Song and Martinez-Sanchez.[9, 10]

Upstream Flow

The upstream flow is steady and irrotational. Therefore, the flowfield obeys Laplace's equation,

$$(c_x, c_y) = \nabla\phi, \qquad \nabla^2\phi = 0 \tag{A1}$$

After azimuthal flow redistribution, the axial velocity is assumed to be

$$c_x(0-, y, t) = \mathrm{Re}\{\bar{c}_{x0} + \hat{K}_0 \exp\{i[(y/R) - \Omega t]\}\} \tag{A2}$$

and

$$c_y(x, y, t) = \mathrm{Re}\{i\hat{K}_0 \exp[x/R + i(y/R - \Omega t)]\} \tag{A3}$$

$$p(x, y, t) = p(-\infty) - \mathrm{Re}\{\rho(\bar{c}_{x0} - i\Omega R)\hat{K}_0 \exp[x/R + i(y/R - \Omega t)]\} \tag{A4}$$

where $\hat{K}_0$ is the complex amplitude of axial velocity perturbation as the flow approaches the disk. From now on, the Re[ ] notation will be dropped for convenience.

Downstream Flow

Just downstream of the actuator disk, the flow consists of two distinct regions: the main passage flow that has traversed the bladed part of the rotor (minus superscript) and the underturned flow (plus superscript) due to the rotor tip gap. The equations of conservation of mass, x momentum, and y momentum can be written for each region. The flow variables are assumed to consist of a mean value plus a small perturbation.

After substitution into the continuity and two-dimensional momentum equations for each stream and linearization of the resulting equations, one can obtain a homogeneous set of equations for eigenvalues and eigenvectors. Then, the nontrivial homogeneous solution to the system of equations for downstream flow can be written as

$$\left(\hat{c}_x^+, \hat{c}_y^+, \hat{c}_x^-, \hat{c}_y^-, \hat{\Delta}, \frac{\hat{p}}{\rho}\right) = \sum_{i=1}^{5} \hat{K}_i \boldsymbol{E}_i \tag{A5}$$

where the complex constants $\hat{K}_i$ have to be determined. Δ is the thickness of the underturned layer.

Upstream–Downstream Coupling

The blade-scale analysis relates the flow variables at $x = 0-$ to those at $x = 0+$. The far-upstream and far-downstream values of flow variables determined from the blade-scale analysis are equivalent to the same flow variables at $x = 0-$ and $0+$, respectively, on the radius scale. Then the perturbation quantities on the radius scale at $x = 0+$ are related to those on the blade scale at station 4 as

$$\begin{bmatrix} \hat{c}_x^+ \\ \hat{c}_y^+ \\ \hat{c}_x^- \\ \hat{c}_y^- \\ \hat{\Delta} \\ \hat{p}/\rho \end{bmatrix}_{x=0+} = \left[\frac{\hat{c}_x(0-)}{U}\frac{\partial}{\partial\phi} + \frac{\hat{c}_y(0-)}{U}\frac{\partial}{\partial(c_{y0}/U)} + \left(\frac{e}{H}\right)\frac{\partial}{\partial(t/H)}\right] \begin{bmatrix} c_{x4}^+ \\ c_{y4}^+ \\ c_{x4}^- \\ c_{y4}^- \\ \Delta \\ (p_0 - (p_0 - p_4)/\rho) \end{bmatrix} \tag{A6}$$

(radius scale) (blade scale)

where the partial derivatives are to be calculated from the blade-scale analysis.

Now Eqs. (A5) and (A6) can be set equal to each other. Then the terms due to (e/H) act as forcing terms that determine the particular complex amplitudes $\hat{K}_i$. Subsequently, the six perturbation quantities can be determined.

Calculation of Rotordynamic Coefficients

The excitation force coefficients can be obtained from the perturbation quantities of tangential force exerted on the turbine per azimuthal length and average rotor pressure perturbation:

$$f_y' = \bar{\lambda}\bar{q}_{2r}(\bar{c}_{y2r} - \bar{c}_{y3}^+)\left(\frac{\lambda'}{\bar{\lambda}} + \frac{q_{2r}'}{q_{2r}} + \frac{c_{y2r}' - c_{y3}'^+}{\bar{c}_{y2r} - \bar{c}_{y3}^+}\right) + (1 - \bar{\lambda})\bar{q}_{2r}(\bar{c}_{y2r} - \bar{c}_{y3}^-)\left(\frac{-\lambda'}{1 - \bar{\lambda}} + \frac{q_{2r}'}{q_{2r}} + \frac{c_{y2r}' - c_{y3}'^-}{\bar{c}_{y2r} - \bar{c}_{y3}^-}\right) \tag{A7}$$

$$\langle p\rangle' = p_2' - (\rho/2)\left[\tan^2\beta_3 \bar{c}_{x3}^- c_{x3}'^- - (\bar{c}_{y2r} - U)c_{y2r}'\right] \tag{A8}$$

Upon projection onto the whirling frame $X'Y'$, the total nondimensional lateral forces are

$$\left[\frac{F_{Y'}}{(Q/2R)(e/H)} + i\frac{F_{X'}}{(Q/2R)(e/H)}\right]_{\text{total}} = \frac{-\hat{f}_y + iL\langle\hat{p}\rangle}{\bar{f}_y(e/H)} \tag{A9}$$

Acknowledgment

Inha University 1996 Research Grant support is gratefully acknowledged.

References

[1] Ehrich, F. F., and Childs, D. W., "Self-Excited Vibrations in High Performance Turbomachinery," *Mechanical Engineering*, May 1984, pp. 66–79.

[2] Thomas, H. J., "Instabile Eigenschwingungen von Turbinenlaeufern Angefacht durch die Spaltstroemung in Stopfubuchsen und Bechauchflug (Unstable Natural Vibrations of Turbine Rotors Induced by the Clearance Flows in Glands and Blading)," *Bull. de. L.A.I.M.*, Vol. 71, No. 11/12, 1958, pp. 1039–1063.

[3] Alford, J. S., "Protecting Turbomachinery from Self-Excited Rotor Whirl," *Journal of Engineering for Power*, Vol. 87, Oct. 1965, pp. 333, 334.

[4] Millsaps, K. T., "Dynamic Forces from Single Gland Labyrinth Seals: Part I—Ideal and Viscous Decomposition," *Journal of Turbomachinery*, Vol. 116, Oct. 1994, pp. 686–693.

[5] Millsaps, K. T., "Dynamic Forces from Single Gland Labyrinth Seals: Part II—Upstream Coupling," *Journal of Turbomachinery*, Vol. 116, Oct. 1994, pp. 694–700.

[6] Childs, D. W., "Rotordynamic Models for Turbines and Pump Impellers," *Turbomachinery Rotordynamics*, Wiley, New York, 1993, pp. 355–394.

[7] Urlichs, K., "Clearance Flow Generated Transverse Forces at the Rotors of Thermal Turbomachines," NASA TM-77292, Oct. 1983; Translation of Ph.D. Dissertation, Dept. of Mechanical Engineering, Munich Technical Univ., Munich, Germany, 1975.

[8] Martinez-Sanchez, M., Jaroux, B., Song, S. J., and Yoo, S., "Measurement of Turbine Blade–Tip Rotordynamic Excitation Forces," *Journal of Turbomachinery*, Vol. 117, July 1995, pp. 384–393.

[9] Song, S. J., and Martinez-Sanchez, M., "Rotordynamic Forces Due to Turbine Tip Leakage—Part I: Blade Scale Effects," *Journal of Turbomachinery*, Vol. 119, Oct. 1997, pp. 695–703.

[10] Song, S. J., and Martinez-Sanchez, M., "Rotordynamic Forces Due to Turbine Tip Leakage—Part II: Radius Scale Effects and Experimental Verification," *Journal of Turbomachinery*, Vol. 119, Oct. 1997, pp. 704–713.

[11] Ek, E. C., "Solution to the Subsynchronous Whirl Problem in the High Pressure Hydrogen Turbomachinery of the Space Shuttle Main Engines," *Proceedings of the AIAA/ASME/SAE 14th Joint Propulsion Conference* (Las Vegas, NV), AIAA, New York, 1978, pp. 1–24.

R. W. Wlezien
Associate Editor